IEEE Access
Multidisciplinary | Rapid Review | Open Access Journal

Received 15 July 2022, accepted 29 July 2022, date of publication 3 August 2022, date of current version 8 August 2022.

*Digital Object Identifier 10.1109/ACCESS.2022.3196025*

RESEARCH ARTICLE

# Decoupling Hybrid Metal Walls and Half-Wavelength Diagonal Open-Slots Based Four-Port Square Patch Antenna With High Port Isolation and Low Radiation Correlation for 2.4/5/6 GHz WiFi-6E 4 × 4 MIMO Access Points

**KIN-LU WONG[1], (Fellow, IEEE), HONG-YU JIANG[1], (Student Member, IEEE), AND WEI-YU LI[2], (Member, IEEE)**

[1]Department of Electrical Engineering, National Sun Yat-sen University, Kaohsiung 80424, Taiwan
[2]Information and Communications Research Laboratories, Industrial Technology Research Institute, Hsinchu 31057, Taiwan

Corresponding author: Kin-Lu Wong (wongkl@mail.nsysu.edu.tw)

This work was supported by the Ministry of Science and Technology, Taiwan, under Grant MOST 111-2218-E-110-003.

**ABSTRACT** Based on applying the hybrid metal walls and half-wavelength diagonal open-slots, a four-port square patch antenna (SPA) having high port isolation (>20 dB) and low radiation correlation (envelope correlation coefficients < 0.01) for 2.4/5/6 GHz (2.4-2.5/5.15-7.125 GHz) WiFi-6E 4 ×4 MIMO access-point application is presented. The four-port SPA is an all-metal structure with a small-size square patch (50 mm × 50 mm, about 0.41λ × 0.41λ at 2.45 GHz) mounted 11 mm above a ground plane. Between the square patch and the ground plane, the hybrid metal walls consisting of an outer shorting metal wall and an inner gap-coupled metal wall are placed along the patch's two centerlines to create four isolated resonant quadrants for the four ports. Each resonant quadrant can support the $TM_{1/2,1/2}$ mode or the $TM_{1/2,1/2}$-like mode in the 2.4 GHz and 5/6 GHz bands. Owing to the inner gap-coupled metal wall, enhanced port isolation between two adjacent ports can be obtained. Additionally, enhanced port isolation between two opposite ports is obtained by embedding two half-wavelength open-slots (length about 0.5λ at 2.45 GHz) along the patch's two diagonal lines. The decoupling hybrid metal walls and half-wavelength diagonal open-slots together enhance the port isolation of the four ports to be larger than 20 dB over the 2.4 GHz and 5/6 GHz bands. The antenna structure and operation principle of the proposed four-port SPA are described. Experimental results of the fabricated prototype are also presented.

**INDEX TERMS** Four-port square patch MIMO antennas, WiFi-6E MIMO access-point antennas, gap-coupled metal walls, decoupling half-wavelength open-slots, 4 × 4 MIMO antennas.

## I. INTRODUCTION

For 4 × 4 multi-input-multi-output (MIMO) access-point antenna applications, the four-port single-patch antennas with high port isolation to generate four uncorrelated waves have been shown to be promising [1]–[4]. This kind of four-port single-patch antennas is attractive for their compact MIMO antenna structure, which can be applied to decrease the required size of the MIMO array [1]. In order to achieve high port isolation for the four ports co-located in a single patch and to obtain low correlation for the four radiated waves, the studies in [1], [2] applied the technique based on the theory of the characteristic mode to design multimode antennas [5].

In [1], the four ports in a square patch excite four different sets of orthogonal characteristic modes to achieve high port isolation (> 20 dB) and wideband operation (6.0-8.5 GHz,

The associate editor coordinating the review of this manuscript and approving it for publication was Ladislau Matekovits.

fractional bandwidth 34.5%). In [2], the four ports collocated in a hexagonal patch can also achieve high port isolation and wideband operation (3.0-6.0 GHz, 66.7%). However, to obtain high port isolation, both antenna designs [1], [2] require using a large-size external feed network, which will increase the power loss and complicate the antenna design. In addition, the required patch size is also larger ($0.85\lambda \times 0.85\lambda$ [1], $1.10\lambda \times 1.10\lambda$ [2]; $\lambda$ is the wavelength of the center frequency in the respective operating band) to achieve the high port isolation. Also, both designs use a very high profile above the ground plane ($0.38\lambda$ [1], $0.34\lambda$ [2]; $\lambda$ is the wavelength of the central operating frequency) to obtain the corresponding wideband operation.

On the other hand, both designs in [3], [4] require no external feed circuitry to achieve enhanced port isolation of the four ports. The antenna structures are therefore simpler than those in [1], [2]. The four-port single-patch antenna in [3] uses the gap-coupled shorting strips to separate an annular-ring patch into four isolated one-quarter arc sections to generate the monopolar patch antenna mode [6] for each port. The port isolation is better than 15 dB over the wideband of 3.3-5.0 GHz (41% in fractional bandwidth) and the envelope correlation coefficients (ECCs) for the four radiated waves are lower than 0.05. The required patch size is $0.77\lambda \times 0.77\lambda$ and the antenna height is 10 mm ($0.14\lambda$, $\lambda$ is the wavelength at 4.15 GHz, the central operating frequency) [3].

For the design in [4], the shorting metal walls are applied to a square patch antenna to create four isolated quarter-wavelength resonant quadrants to generate the $TM_{1/2,1/2}$ mode for each port. With a patch size of $0.58\lambda \times 0.58\lambda$ and an antenna height of 10 mm ($0.14\lambda$, $\lambda$ is the wavelength at 4.15 GHz), the port isolation better than 15 dB over the wideband of 3.3-5.0 GHz (41%) can also be obtained. The comparison of the above four-port single-patch antennas with four uncorrelated waves for MIMO access-point applications is also listed in Table 1.

It is also noted that the designs in [1]–[4] require using the dielectric substrate layer to support the feed network or the radiating patch. The use of the dielectric substrate for the access-point antennas is less attractive for practical applications. In addition, although the designs in [3], [4] are simpler in antenna structure and smaller in antenna size, the obtained port isolation ($>$ 15 dB) over the wideband is lower than that ($>$ 20 dB) of the designs in [1], [2].

Other than the four-port single-patch antennas [1]–[4] suitable for MIMO access-point applications with primarily front-semispherical radiation, there are also reported four-port MIMO antennas based on the printed monopole or slot antenna elements, such as in [7]–[11]. These four-port antennas show bidirectional radiation, different from the patch antennas studied here and in [1]–[4].

The four-port printed patch antennas with a defected ground plane for enhanced port isolation have also been reported [12]–[14]. These antennas are more suitable for mobile MIMO antenna applications. There are also low-profile four-port open-slot antennas backed by a ground plane [15] or low-profile four-port patch antennas [16]–[19] reported mainly for the smartphone or mobile device antenna applications, which however are not suitable for MIMO access-point antennas [1]–[4].

**TABLE 1. Comparison of the four-port single-patch antennas with four uncorrelated waves for MIMO access-point applications.**

| Ref. | [1] | [2] | [3] | [4] | This work |
|---|---|---|---|---|---|
| Antenna height | 15.7mm (0.38λ@ 7.25GHz) | 23mm (0.34λ@ 4.5GHz) | 10mm (0.14λ@ 4.15GHz) | 10mm (0.14λ@ 4.15GHz) | 11.2mm (0.09λ@ 2.45GHz) |
| Patch size | 0.85λ x 0.85λ | 1.10λ x 1.10λ | 0.77λ x 0.77λ | 0.58λ x 0.58λ | 0.41λ x 0.41λ |
| Operating bandwidth | Wide-band 6-8.5GHz (35%) | Wide-band 3-6GHz (67%) | Wide-band 3.3-5GHz (41%) | Wide-band 3.3-5GHz (41%) | Dual-band 2.4-2.5GHz/ 5.1-7.2GHz (4.1%/34%) |
| Antenna efficiency | > 70% | Not given | > 84% | > 83% | > 86%/90% in low/high band |
| ECC | < 0.01 | Not given | < 0.05 | < 0.03 | < 0.01 |
| Port isolation | > 20 dB | > 20 dB | > 15 dB | > 15 dB | > 20 dB in low/high band |
| External feed network | Yes, for high port isolation | Yes, for high port isolation | No | No | No |
| All-metal structure | No | No | No | No | Yes |

In this study, for WiFi-6E MIMO access-point applications, an all-metal four-port single-patch antenna with no external feed network required as in [1], [2] and having a smaller antenna size with respect to the operating wavelength than those in [1]–[4] to achieve high port isolation ($>$ 20 dB) and low radiation correlation (ECC $<$ 0.01) is presented. The proposed design is a four-port square patch antenna (SPA) in which the decoupling techniques of applying the hybrid metal walls and half-wavelength diagonal open-slots are proposed to obtain high port isolation of the four ports. The proposed design operates in dual bands of bandwidths larger than 2.4-2.5 GHz (4.1%) and 5.1-7.2 GHz (34%) and can cover the 2.4 GHz (2.4-2.5 GHz) and 5/6 GHz (5.15-7.125 GHz) WiFi-6E bands [20]–[23] for $4 \times 4$ MIMO access-point application.

In addition, the proposed four-port SPA is an all-metal structure with a small-size square patch of 50 mm $\times$ 50 mm (about $0.41\lambda \times 0.41\lambda$ at 2.45 GHz) mounted 11.2 mm (about $0.09\lambda$ at 2.45 GHz) above the ground plane. The required antenna size is also smaller than those in [1]–[4] (see the comparison summarized in Table 1).

Details of the proposed four-port SPA are described. The operating principle of the decoupling techniques applied in the proposed design is addressed. A parametric study for adjusting the impedance matching and transmission coefficients of the four ports in the proposed design is conducted. Experimental results of the fabricated four-port SPA are also presented and discussed.

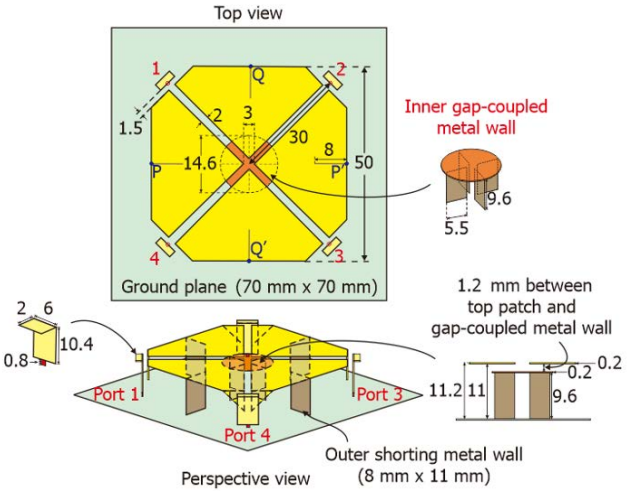


**FIGURE 1.** Proposed four-port (Ports 1-4) single-patch WiFi-6E MIMO antenna with high port isolation.

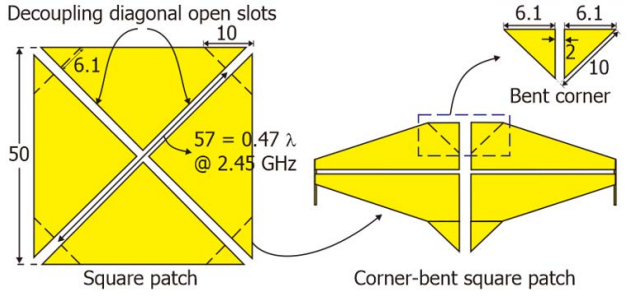


**FIGURE 2.** Schematic diagram for bending the four corners of the square patch in the proposed antenna.

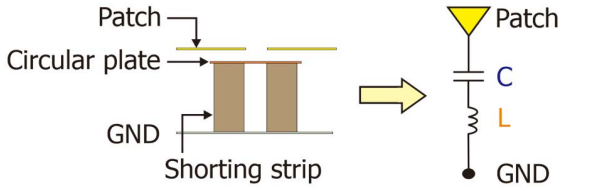


**FIGURE 3.** Equivalent circuit diagram of the inner gap-coupled metal wall.

## II. ANTENAN STRUCTURE AND OPERATION STUDY

Fig. 1 shows the proposed four-port (Ports 1-4) single-patch WiFi-6E MIMO antenna with high port isolation. The antenna is an all-metal structure formed by using a four-corner-bent square patch connected or coupled through four hybrid metal walls located along the patch's two centerlines (PP', QQ') to the antenna's ground plane. Each hybrid metal wall is placed along the centerline of the square patch and consists of an outer shorting metal wall and an inner gap-coupled metal wall. The hybrid metal walls separate the region between the square patch and the ground plane into four 90° resonant quadrants. Each resonant quadrant is bounded by two orthogonal hybrid metal walls, and two adjacent resonant quadrants share a same hybrid metal wall.

Two open-slots of width 2 mm are also embedded along the patch's two diagonal lines. At four ends of the two diagonal open-slots locate four coupling feeds (namely, Ports 1-4 in the proposed antenna). Each coupling feed uses an inverted-L strip to capacitively excite each resonant quadrant bounded by two orthogonal metal walls to generate the $TM_{1/2,1/2}$ mode (the resonant mode with two orthogonal quarter-wavelength resonances) [4], [24] and the $TM_{1/2,1/2}$-like mode, respectively, in the desired 2.4 GHz band (2.4-2.5 GHz) and 5/6 GHz band (5.15-7.125 GHz) for WiFi-6E applications. Note that the square patch, hybrid metal walls, ground plane, and coupling feed strips all uses 0.2 mm thick copper plates in the proposed antenna.

The square patch has a small size of 50 mm × 50 mm (about 0.41λ × 0.41λ at 2.45 GHz) and the antenna height is 11.2 mm (about 0.09λ at 2.45 GHz). The ground plane is in a square shape of side length 70 mm (about 0.57λ or larger than a half-wavelength at 2.45 GHz). The coupling feed strip has a vertical strip (6 mm × 10.4 mm) and a horizontal strip (6 mm × 2 mm) extended opposite to the square patch. For each port, the vertical strip couples through a gap of 1.5 mm to the patch's bent section at each corner, thereby to excite the $TM_{1/2,1/2}$ mode or the $TM_{1/2,1/2}$-like mode supported by each resonant quadrant. The schematic diagram showing the bending of the patch's four corners in the proposed antenna is also illustrated in Fig. 2. The dimensions of the bent section at each corner are shown in the figure.

Note that, by bending the patch corners whose side length is 10 mm, the length of each diagonal open-slot in the top square patch is adjusted to be 57 mm (about 0.47 at 2.45 GHz, close to a half-wavelength). The half-wavelength diagonal open-slot can lead to a dip in the transmission coefficient of two opposite ports (Ports 1, 3 or Ports 2, 4) at about 2.45 GHz, thereby greatly enhancing the port isolation of two opposite ports to be larger than 20 dB in the 2.4 GHz band.

When the effective length of the diagonal open-slots is varied, the dip of the transmission coefficients of two opposite ports will also be varied. This behavior is found to be similar to that of the half-wavelength closed-slot working as a band-notching element [25]. More results of the decoupling half-wavelength diagonal open-slot are presented in the parametric study.

On the other hand, by applying the hybrid metal walls, the transmission coefficient of two adjacent ports (Ports 1, 2 or Ports 2, 3 or Ports 3, 4 or Ports 1, 4) can also have a dip at about 2.45 GHz, which in turn leads to high port isolation of larger than 20 dB for two adjacent ports in the 2.4 GHz band. For the port isolation in the 5/6 GHz band, owing to the relatively much smaller wavelength, the distances between the four ports are much larger than those in the 2.4 GHz band. High port isolation of the four ports in the 5/6 GHz band is also observed. Therefore, with the combined effects of the half-wavelength diagonal open-slots and the hybrid metal walls, high port isolation of all the four ports in the 2.4 GHz and 5/6 GHz bands is obtained for the proposed antenna.

Note that, in each 90° resonant quadrant, the outer shorting metal wall of the hybrid metal wall has a size of 8 mm × 11 mm to directly connect the square patch to the ground plane. For each port, good resonant quadrant bounded by two metal walls can therefore be obtained in both the 2.4 and

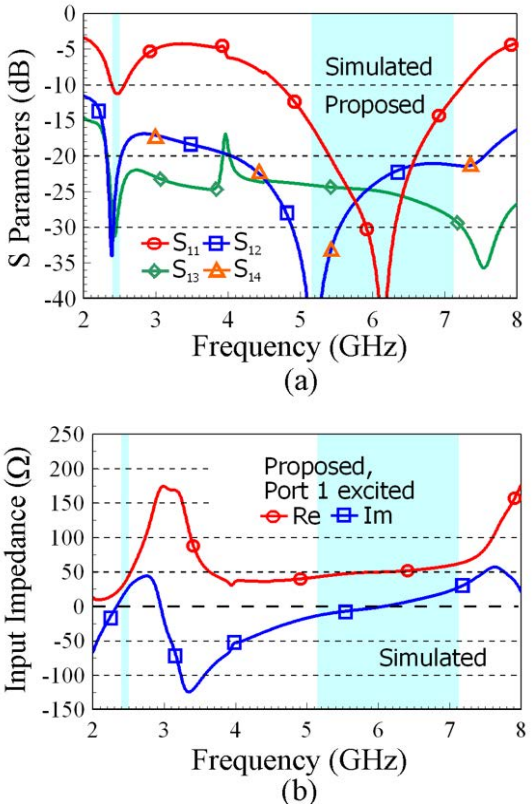


**FIGURE 4.** Simulated (a) S parameters and (b) input impedance of Port 1 excited in the proposed antenna.

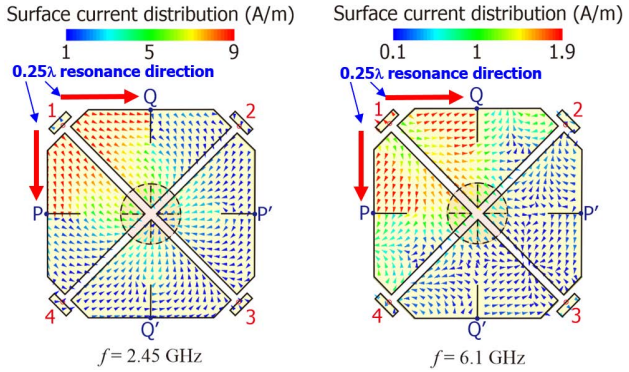


**FIGURE 5.** Simulated vector surface current distributions at 2.45 GHz and 6.1 GHz for Port 1 excited in the proposed antenna.

5/6 GHz bands. While in each resonant quadrant, the inner gap-coupled metal wall consists of a vertical shorting strip (5.5 mm × 9.6 mm) and a circular plate (diameter 14.6 mm) coupled through a 1.2 mm gap to the square patch. The gap-coupled metal wall is considered to function like a series *LC* structure or a band-pass resonant structure [26], [27] with a center frequency at about 2.45 GHz. The equivalent circuit diagram of the gap-coupled metal wall is shown in Fig. 3.

With the aid of the flat wire inductor calculator [28], the equivalent inductance of the vertical shorting strip is evaluated to be about 3.55 nH ($L$). That is, it will have an equivalent inductive reactance of about j54.6 Ω ($j\omega L$) at 2.45 GHz. On the other hand, the equivalent series capacitance between

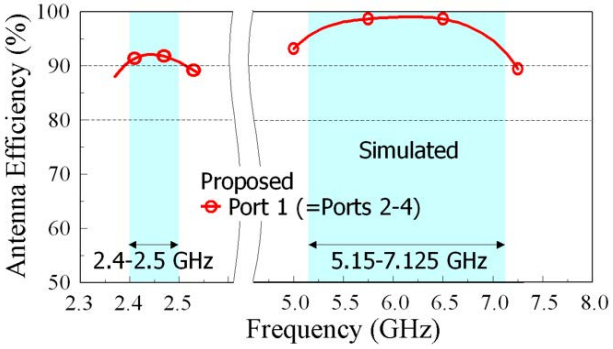


**FIGURE 6.** Simulated antenna efficiency of Port 1 excited in the proposed antenna.

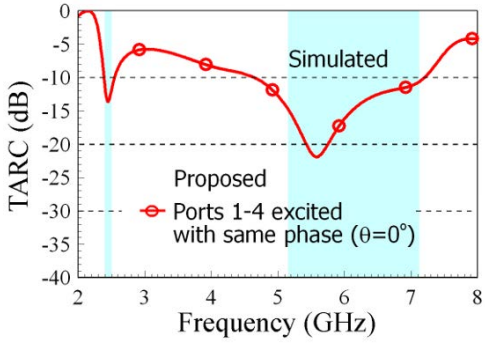


**FIGURE 7.** Simulated total active reflection coefficient (TARC) for the proposed antenna.

the circular plate and the square patch is calculated to be about 1.23 pF ($C$), which will contribute to an equivalent capacitive reactance of about -j52.8 Ω ($1/j\omega C$). The series *LC* circuit can therefore have a resonant frequency $[1/(2\pi(LC)^{-1/2})]$ at about 2.45 GHz, at which the gap-coupled metal wall is expected to exhibit a zero or close-to-zero impedance. In this case, the surface current on the excited patch quadrant coupled to adjacent patch quadrants will be effectively detoured from originally toward the adjacent ports to toward the patch center where the gap-coupled metal wall is located. Enhanced port isolation of the adjacent ports in the 2.4 GHz band can thus be obtained.

Note that when the gap-coupled structure is not applied, the simple shorting strip or the shorting metal wall will have a relatively much larger reactance than that of the gap-coupled metal wall at resonance. In this case, the simple shorting metal wall cannot achieve the same function of attracting the surface current on the excited patch quadrant as the gap-coupled metal wall.

On the other hand, owing to the higher operating frequencies in the 5/6 GHz band, the equivalent series capacitor in the gap-coupled metal wall will have a lower capacitive reactance than in the 2.4 GHz band. That is, in the 5/6 GHz band, the gap-coupled metal wall will be expected to function more like a direct-connect metal wall, similar to the outer shorting metal wall. This indicates that the port isolation in the 5/6 GHz band will be relatively very slightly affected by the inner gap-coupled metal wall. More results of the decoupling gap-coupled metal wall will be presented later.

Based on the proposed antenna in Fig. 1, the simulated results obtained by using the commercially available three-dimensional (3D) High Frequency Electromagnetic Simulation Software (ANSYS HFSS) [29] are presented. Fig. 4 shows the simulated *S* parameters and input impedance of Port 1 excited in the proposed antenna. Note that the corresponding results of Ports 2-4 are same as that of Port 1, owing to the symmetric structure of the proposed antenna. As seen in Fig. 4(a), over the desired 2.4 GHz and 5/6 GHz bands (see the colored frequency regions of 2.4-2.5 GHz and 5.15-7.125 GHz in the figure), the impedance matching is less than -10 dB. The transmission coefficients of Port 1 to Ports 2-4 are less than -20 dB, indicating that high port isolation of larger than 20 dB is obtained for the four ports in the proposed antenna.

Also note that both the $S_{12}$ ($=S_{14}$) for two adjacent ports and the $S_{13}$ for two opposite ports have a dip at about 2.4 GHz. This behavior is owing to the presence of the decoupling half-wavelength diagonal open-slots and hybrid metal wall. The simulated input impedance of Port 1 shown in Fig. 4(b) indicates that two resonances (zero input reactance) occur at about 2.4 GHz and 6.1 GHz. Also, relatively very smooth variations in the input resistance in the 5/6 GHz band is seen. This accounts for the obtained wideband operation (high-band bandwidth larger than 2 GHz) of the proposed antenna to cover the 5/6 GHz for WiFi-6E application.

To analyze the two resonant modes excited for the 2.4 GHz and 5/6 GHz bands, the simulated vector surface current distributions at 2.45 GHz and 6.1 GHz for Port 1 excited in the proposed antenna are shown in Fig. 5. Similar surface current distributions are seen for both frequencies. The surface currents are seen to be symmetric with respect to the diagonal open-slot in the resonant quadrant of Port 1.

Additionally, the surface currents are generally directed toward the two orthogonal outer shorting metal walls (see the red arrows indicating the 0.25λ resonance direction along two orthogonal patch edge directions in the figure). This type of surface current distributions with two orthogonal 0.25λ resonances excitation is similar to that of the $TM_{1/2,1/2}$ mode [4], [24] for the resonant cavity of the patch antenna bounded by two orthogonal metal walls. The resonant mode for the 2.4 GHz band is therefore denoted as the $TM_{1/2,1/2}$ mode here.

On the other hand, the resonant mode for the 5/6 GHz band is denoted as the $TM_{1/2,1/2}$-like mode here. This is to consider that, at 6.1 GHz, its excited surface currents near the coupling feed are slightly modified owing to the coupling feed strip having a length of about 12.4 mm (10.4 mm for its vertical height plus 2 mm for its horizontal extended length), close to 0.25λ at 6.1 GHz. The coupling feed strip will therefore be expected to contribute to the antenna radiation at around 6.1 GHz. This also helps in obtaining the wide high band of the proposed antenna.

Fig. 6 shows the simulated antenna efficiency of Port 1 excited in the proposed antenna. The simulated antenna efficiency includes the mismatching loss. The antenna

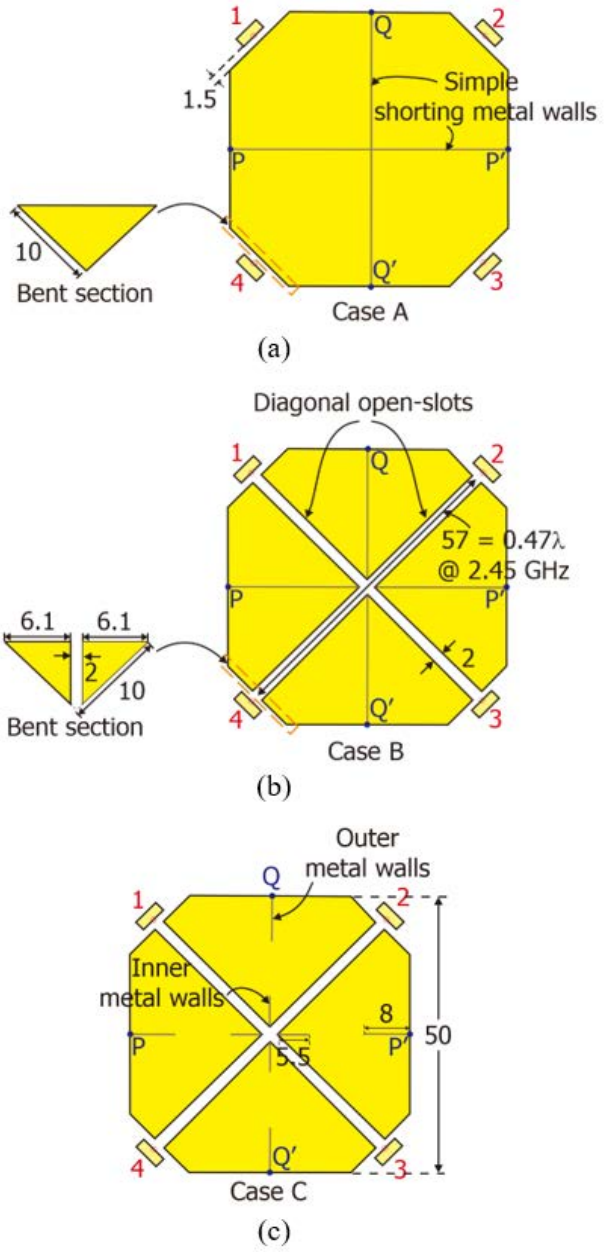


**FIGURE 8.** Geometries of (a) the case with simple shorting metal walls and no diagonal open-slots (Case A), (b) Case A with diagonal open-slots (Case B), and (c) Case B with discrete (inner and outer) shorting metal walls (Case C). Corresponding dimensions are same as those shown in Fig. 1 for the proposed antenna.

efficiency reaches about 90% in the 2.4 GHz band and is larger than 92% in the 5/6 GHz band. That is, high antenna efficiencies of Ports 1-4 are obtained, which is owing to the high port isolation and good impedance matching obtained for the proposed antenna in the 2.4 GHz and 5/6 GHz bands.

Furthermore, to consider Ports 1-4 of the proposed antenna to operate at the same time for MIMO operation, the simulated total active reflection coefficient (TARC) [30], [31] is presented in Fig. 7. For considering Ports 1-4 to transmit four synchronized MIMO signal streams with same amplitudes and phases, the obtained TARC values are seen to be less than

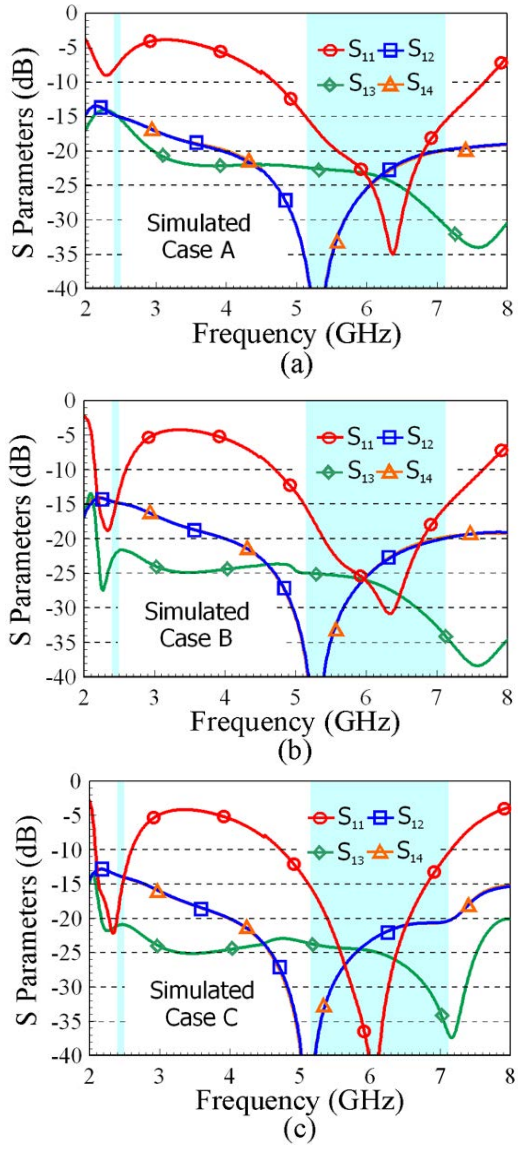


**FIGURE 9.** Simulated S parameters of Port 1 excited in Cases A, B, and C. (a) Case A. (b) Case B. (c) Case C.

−10 dB in the 2.4 GHz and 5/6 GHz bands. That is, the active reflection coefficients obtained by considering the four ports as a whole are also good for practical applications. This may also be owing to the high isolation of the four ports in the proposed antenna.

## III. DESIGN CONSIDERATIONS

To further demonstrate the design considerations of the proposed antenna, Fig. 8 shows three geometries of Cases A, B, and C. The case with simple shorting metal walls and no diagonal open-slots is denoted as Case A in Fig. 8(a). Case A can be considered as the initial design of the proposed antenna without the proposed decoupling structures in this study. Case B in Fig. 8(b) is formed by adding diagonal open-slots to Case A. Case C in Fig. 8(c) is obtained by using discrete (inner and outer) shorting metal walls in Case B.

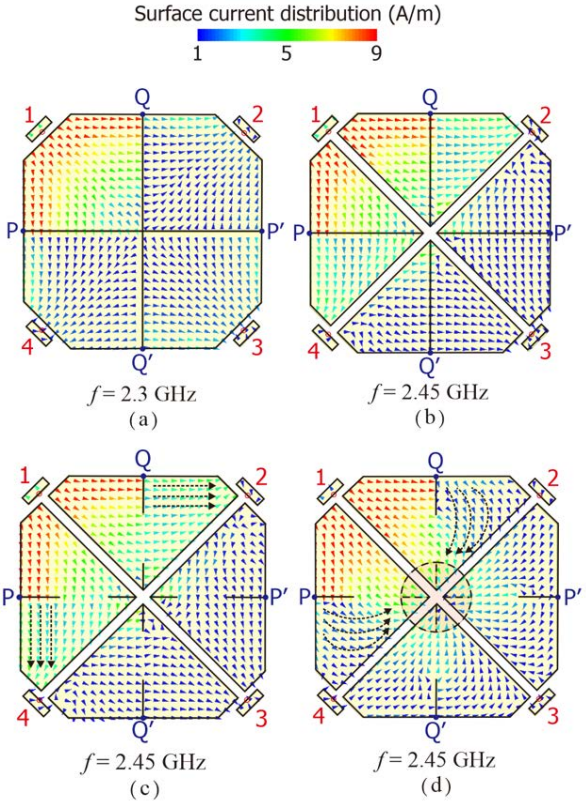


**FIGURE 10.** Comparison of the simulated vector surface current distributions for Port 1 excitation. (a) 2.30 GHz, Case A. (b) 2.45 GHz, Case B. (c) 2.45 GHz, Case C. (d) 2.45 GHz, Proposed.

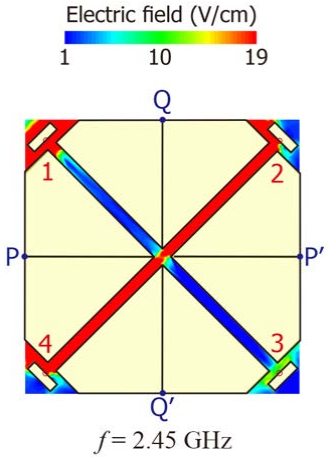


**FIGURE 11.** Simulated electric field distributions in the plane of the square patch for Port 1 excited in Case B at 2.45 GHz.

Corresponding dimensions of the three cases are same as those shown in Fig. 1 for the proposed antenna.

For comparison, Fig. 9 shows the simulated *S* parameters of Port 1 excited in Cases A, B, and C. The obtained *S* parameters of Case A in Fig. 9(a) show that the port isolation in the antenna's low band is less than 15 dB, while that in the antenna's high band (5/6 GHz band) is larger than 20 dB.

Note that the resonant mode excited in the antenna's low band in Case A occurs at a frequency lower than 2.4 GHz. This is because the antenna dimensions in Case A are kept as

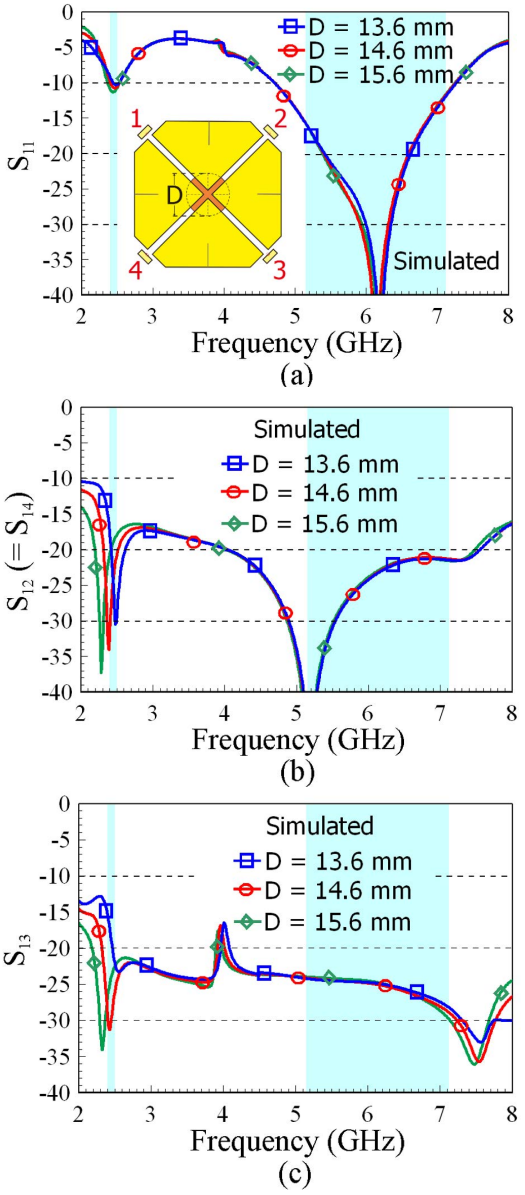


**FIGURE 12.** Simulated S parameters of Port 1 for varying the circular plate diameter (D) of the inner gap-coupled metal wall. (a) $S_{11}$. (b) $S_{12}$ (= $S_{14}$). (c) $S_{13}$. Other dimensions are fixed as in Fig. 1.

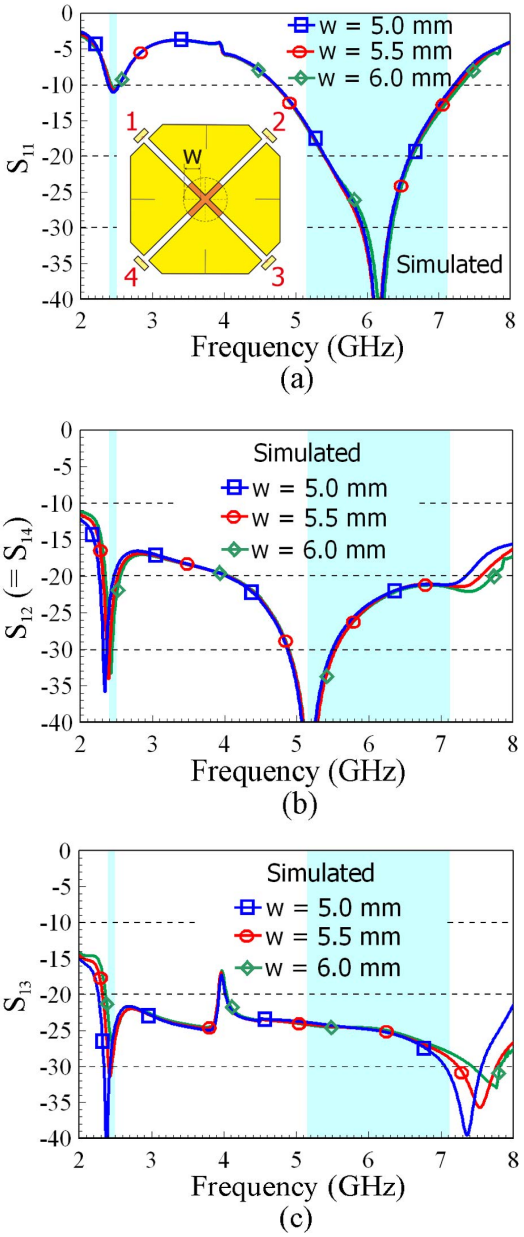


**FIGURE 13.** Simulated S parameters of Port 1 for varying the shorting strip width (w) of the inner gap-coupled metal wall. (a) $S_{11}$. (b) $S_{12}$ (= $S_{14}$). (c) $S_{13}$. Other dimensions are fixed as in Fig. 1.

same as those in the proposed antenna. By slightly adjusting the design dimensions in Case A, its low band can be adjusted to cover the 2.4 GHz band. However, the port isolation in its low band will still be lower than about 15 dB.

In Fig. 9(b), it is observed that a dip in the $S_{13}$ of Ports 1 and 3 (two opposite ports) is obtained in the antenna's low band, which greatly enhances the isolation of two opposite ports in the 2.4 GHz band to be larger than 20 dB. In addition, the impedance matching in the antenna's low band is improved. The results are attributed to the presence of decoupling half-wavelength diagonal open-slots in Case B. The dip in the $S_{13}$ can be adjusted when the effective length of the diagonal open-slots is varied. Also, very slight effects in the $S$ parameters of the antenna's high band are seen. The isolation of Ports 1 and 2 or Ports 1 and 4, however, is not improved in the antenna's low band [see the $S_{12}$ (=$S_{14}$) in the figure].

By comparing to the results shown in Fig. 4(a) for the proposed antenna in which the $S_{13}$ and the $S_{12}$ (= $S_{14}$) are all greatly improved to be larger than 20 dB in the 2.4 GHz band. The enhanced isolation of two adjacent ports is owing to the inner gap-coupled metal walls applied in the proposed antenna. Its decoupling principle as a series *LC* structure or a band-pass resonant structure has been addressed in Section II.

When both the inner and outer metal walls use the same simple shorting metal plates (that is, Case C here), the obtained $S$ parameters shown in Fig. 9(c) are similar to those for Case B in Fig. 9(b). Then, by replacing the inner shorting

metal plate with the gap-coupled metal wall introduced in the study, the proposed antenna in Fig. 1 is obtained.

Fig. 10 shows the comparison of the simulated vector surface current distributions for Port 1 excitation in the low band of Cases A-C and the proposed antenna. The surface current distributions in the resonant quadrant of Port 1 in Fig. 10(a) for Case A and in Fig. 10(b) for Case B are seen to be very similar. This confirms that the adding of the diagonal open-slots generally does not affect the resonant mode excitation of the proposed antenna. Also note that the surface current distribution in Fig. 10(a) can be considered to be a close-to-ideal $TM_{1/2,1/2}$ mode. Since the surface current distributions at 2.45 GHz and 6.1 GHz shown in Fig. 5 are very similar to that in Fig. 10(a), the obtained modes of the proposed antenna are denoted as the $TM_{1/2,1/2}$ mode as discussed earlier.

In addition, from the simulated electric field distributions in the plane of the square patch at 2.45 GHz for Port 1 in Case B (see Fig. 11), very strong electric fields occur along the diagonal open-slot with Ports 1 and 3 at its two opposite sides. This causes relatively very weak electric field seen at Port 3. This is mainly owing to the effective length of the diagonal open-slot being about a half-wavelength at 2.45 GHz, thereby causing a dip in the $S_{13}$ in the 2.4 GHz band. High isolation of two opposite ports is therefore obtained.

On the other hand, by comparing the results in Fig. 10(c) and (d), the surface current distributions on the adjacent patch quadrants of Port 1 are detoured from toward Ports 2 and 4 in Case C to toward the patch center for the proposed antenna. This also confirms that the applied gap-coupled metal wall in the proposed antenna can lead to enhanced isolation of two adjacent ports in the antenna's low band or the 2.4 GHz band.

## IV. PARAMETRIC STUDY

To demonstrate the fine adjustment of the port isolation and impedance matching of the proposed antenna, a parametric study is conducted. Fig. 12 shows the simulated $S$ parameters of Port 1 for varying the circular plate diameter ($D$) of the inner gap-coupled metal wall. The results for $D$ varied from 13.6 mm to 15.6 mm are presented. Very small effects on the $S_{11}$ are seen in Fig. 12(a). For the $S_{12}$ (=$S_{14}$) of two adjacent ports shown in Fig. 12(b), the dip in the antenna's low band is shifted to lower frequencies with an increase in the circular plate diameter. This is reasonable, because a large circular plate diameter increases the equivalent capacitance of the gap-coupled metal wall and therefore decreases the resonant frequency thereof. For the $S_{13}$ shown in Fig. 12(c), similar behavior as the $S_{12}$ (=$S_{14}$) is observed. This may be owing to the effective length of the diagonal open-slots being varied in a similar trend, thereby varying the dip of the $S_{13}$ of two opposite ports as well.

Fig. 13 shows the simulated $S$ parameters of Port 1 for varying the shorting strip width ($w$, varied from 5 mm to 6 mm) of the inner gap-coupled metal wall. Effects on the $S_{11}$ are also very small as shown in Fig. 13(a). The dip of

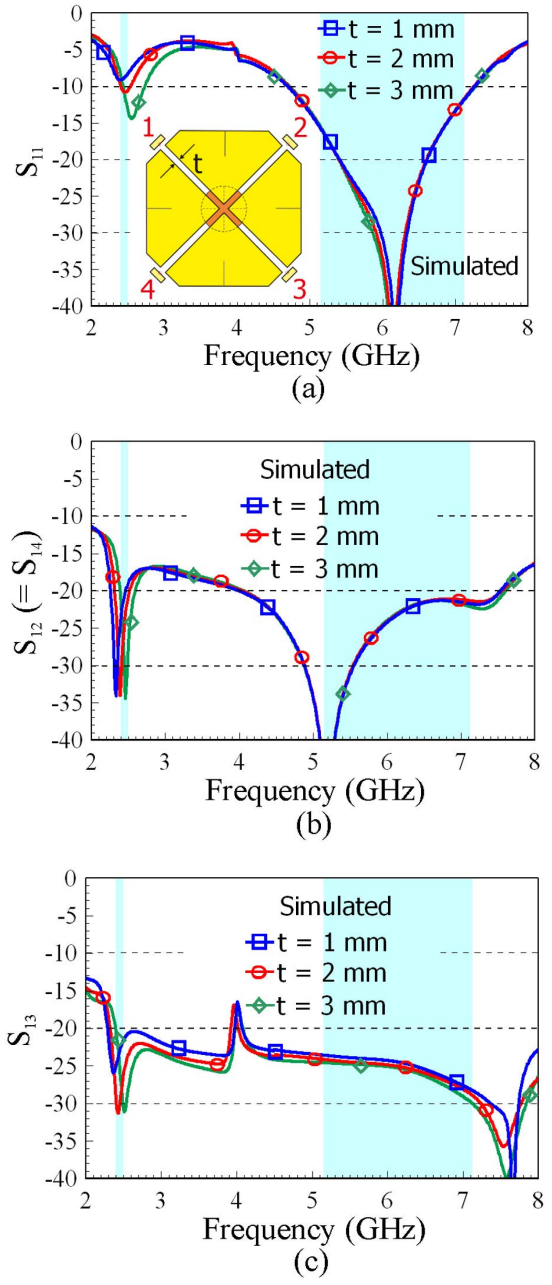


**FIGURE 14.** Simulated S parameters of Port 1 for varying the diagonal open-slot width (t). (a) $S_{11}$. (b) $S_{12}$ (= $S_{14}$). (c) $S_{13}$. Other dimensions are fixed as in Fig. 1.

the $S_{12}$ (=$S_{14}$) shown in Fig. 13(b) is slightly shifted to lower frequencies when the shorting strip width is smaller. Since a smaller shorting strip width leads to a larger equivalent inductance [27], the resonant frequency of the gap-coupled metal wall as a band-pass resonant structure will be decreased. However, the effect is relatively smaller than that of varying the circular plate diameter shown in Fig. 12. Small effects on the $S_{13}$ shown in Fig. 13(c) are also seen.

Effects of varying the diagonal open-slot width ($t$) from 1 mm to 3 mm are shown in Fig. 14. Relatively larger effects on the $S_{11}$ in Fig. 14(a) and the $S_{13}$ in Fig. 14(c) are observed, which are larger than the effects on the $S_{12}$

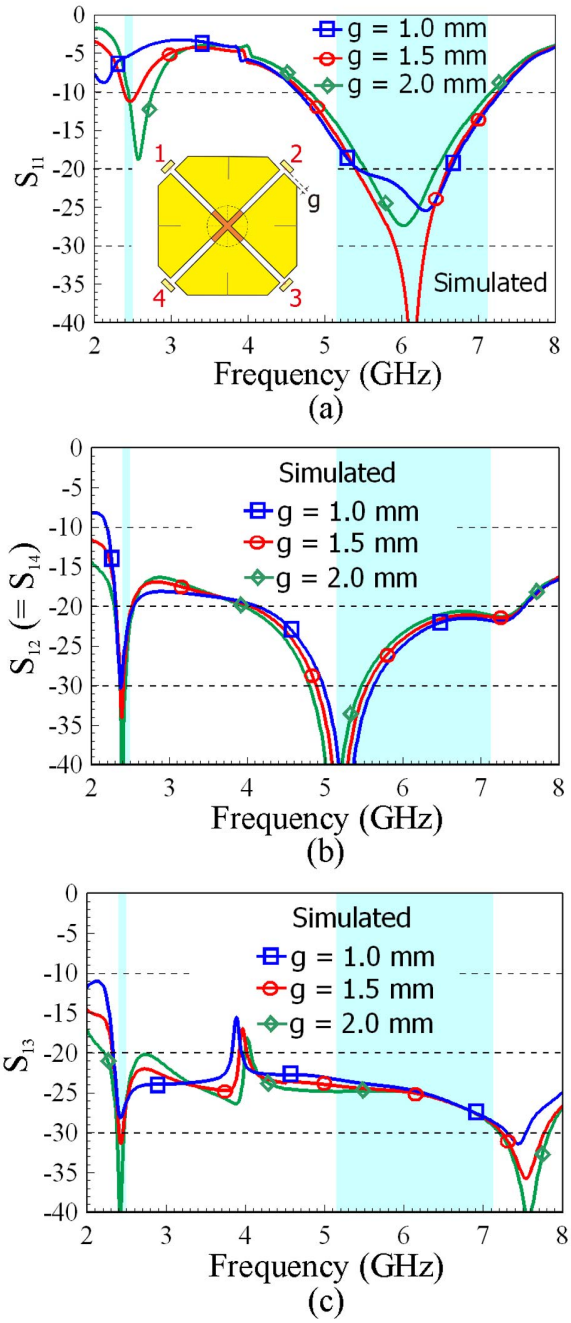


**FIGURE 15.** Simulated S parameters of Port 1 for varying the coupling gap (g) between the L-strip feed and the square patch. (a) $S_{11}$. (b) $S_{12}$ (= $S_{14}$). (c) $S_{13}$. Other dimensions are fixed as in Fig. 1.

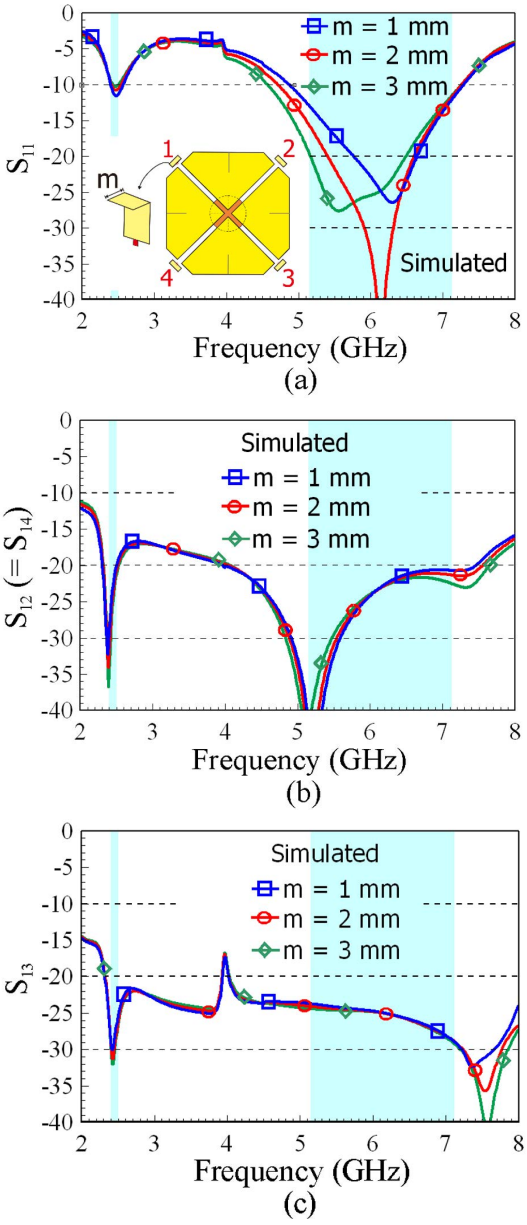


**FIGURE 16.** Simulated S parameters of Port 1 for varying the outward extended length (m) of the L-strip feed's horizontal part. (a) $S_{11}$. (b) $S_{12}$ (= $S_{14}$). (c) $S_{13}$. Other dimensions are fixed as in Fig. 1.

(=$S_{14}$) in Fig. 14(b). This behavior is because the variations in the open-slot width will vary the capacitive coupling of the probe feed and also affect the effective length of the diagonal open-slots.

Fig. 15 shows the simulated $S$ parameters of Port 1 for varying the coupling gap ($g$) between the L-strip feed and the square patch. Small effects on the $S_{12}$ (=$S_{14}$) in Fig. 15(b) and the $S_{13}$ in Fig. 15(c) is seen. On the other hand, relatively larger effects on the $S_{11}$, especially in the antenna's low band, are observed [see Fig. 15(a)]. The results indicate that the impedance matching or reflection coefficients of the proposed antenna can be adjusted by varying the coupling gap ($g$) at each feed, with small effects on the transmission coefficients of the four ports.

To effectively vary the impedance matching in the antenna's high-band or the 5/6 GHz band, Fig. 16 shows the simulated $S$ parameters of Port 1 for varying the outward extended length ($m$) of the L-strip feed's horizontal part from 1 mm to 3 mm. In Fig. 16(a), the $S_{11}$ shows relatively larger effect in the 5/6 GHz band and very small effect in the 2.4 GHz band. Small effects on the $S_{12}$ (=$S_{14}$) and the $S_{13}$ in Fig. 16(b) and (c) are also seen. The relatively larger effect in the 5/6 GHz band is because the feed strip has a length close to a quarter-wavelength at 6.1 GHz and will therefore contribute to the antenna's wide high-band operation. By varying the

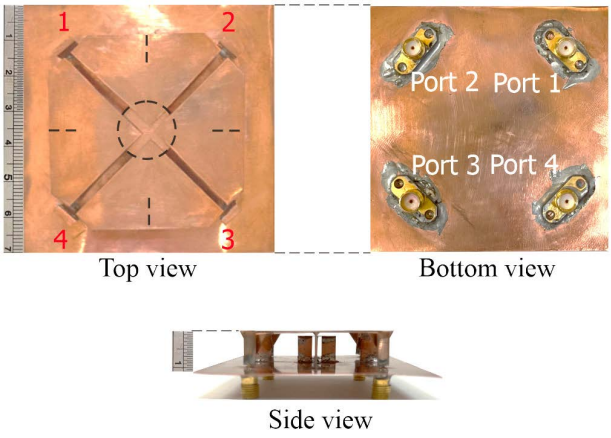


**FIGURE 17.** Fabricated four-port single-patch WiFi-6E MIMO antenna.

length $m$, the total length of the feed strip will be varied, thus causing some variations in the impedance matching in the 5/6 GHz band.

## V. EXPERIMENTAL STUDY

Fig. 17 shows the top, bottom, and side views of the fabricated four-port single-patch WiFi-6E MIMO antenna. The measured $S$ parameters of Ports 1-4 in the fabricated antenna are presented in Fig. 18. The reflection coefficients are shown in Fig. 18(a). The transmission coefficients of two adjacent ports ($S_{12}$, $S_{23}$, $S_{34}$, $S_{14}$) and two opposite ports ($S_{13}$, $S_{24}$) are respectively shown in Fig. 18(b) and (c). The measured results generally agree with the corresponding simulated results included in the figure for comparison. Over the 2.4 GHz and 5/6 GHz bands, the measured reflection coefficients are less than $-10$ dB. For the measured transmission coefficients, they are all less than $-20$ dB. The desired high port isolation is obtained.

Fig. 19(a) and (b) show the measured antenna efficiency and antenna gain of Ports 1-4 in the fabricated antenna. The fabricated antenna was tested in a far-field anechoic chamber and the measured data also generally agree with the corresponding simulated results. A snapshot of the measurement setup of the fabricated antenna in the anechoic chamber is shown in Fig. 20.

The measured antenna efficiency is determined based on integrating the measured radiated electric field intensity over the entire sphere surrounding the tested antenna in the far-field anechoic chamber. The tested antenna is mounted on a two-axis positioner to be rotated from $\theta = 0^{o}$-$180^{o}$ and $\phi = 0^{o}$-$360^{o}$ (generally using $5^{o}$-$10^{o}$ as an interval), with the calibrated horn antenna as the transmitting antenna fixed in the measurement (Great circle test method [32]). The total radiated power can therefore be obtained and the antenna efficiency can be determined.

The obtained measured antenna efficiency of the fabricated antenna is larger than about 86% and 90%, respectively, in the low (2.4 GHz) and high (5/6 GHz) bands. The measured antenna gain is about 4.5-5.0 dBi in the low band and about 4.0-5.9 dBi in the high band.

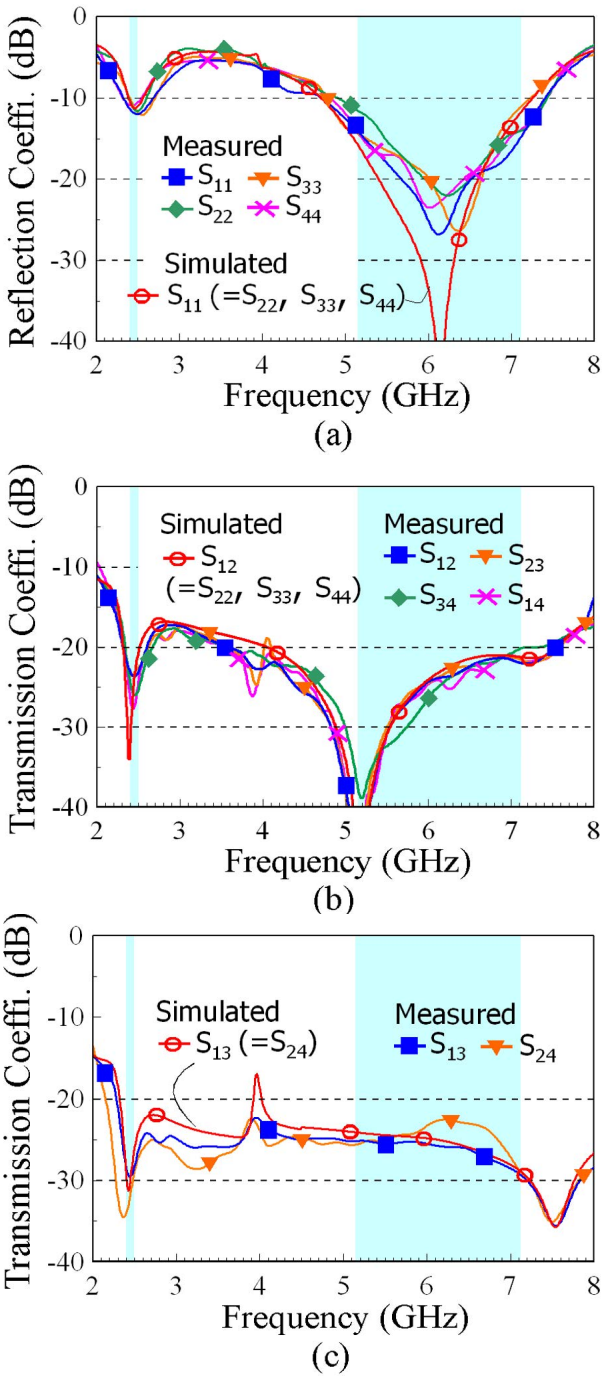


**FIGURE 18.** Measured S parameters of Ports 1-4 in the fabricated antenna. (a) Reflection coefficients. (b) Transmission coefficients of two adjacent ports. (c) Transmission coefficients of two opposite ports. Corresponding simulated results are included.

Also note that, as shown in Fig. 18, although the $S_{11}$ at 2.45 GHz is about -11.5 dB only, the transmission coefficients of Port 1 to Ports 2-4 ($S_{12}$, $S_{13}$, $S_{14}$) are lower than about -24 dB. With the very high port isolation obtained, the measured antenna efficiency at 2.45 GHz is about 88%. When the $S_{11}$ at 2.45 GHz can be further decreased, with high port isolation still obtained, even better antenna performance can be expected.

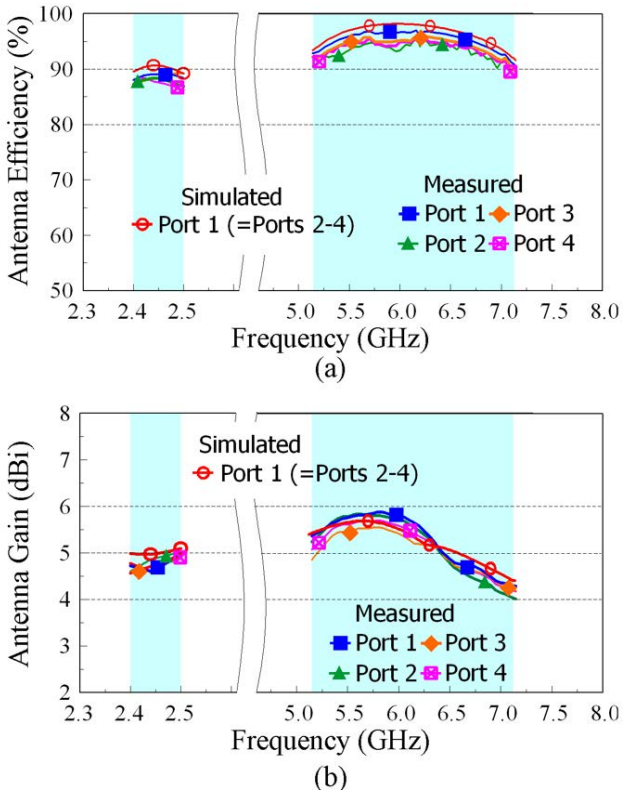


**FIGURE 19.** Measured (a) antenna efficiency and (b) antenna gain of Ports 1-4 in the fabricated antenna. Simulated results of Port 1 are included for comparison.

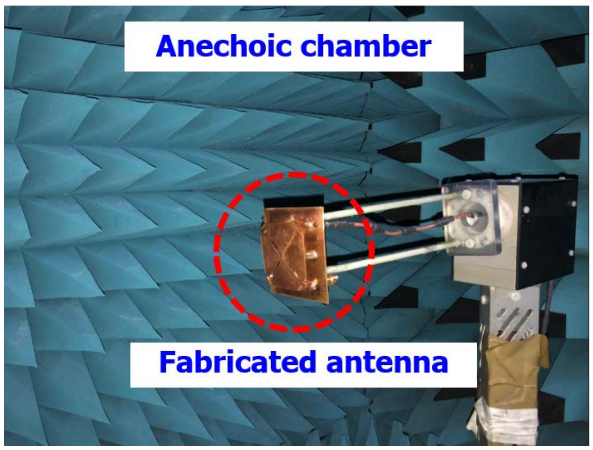


**FIGURE 20.** Measurement setup of the fabricated antenna in the anechoic chamber.

Fig. 21 shows the measured and simulated normalized radiation patterns of Port 1. The results in two principal planes (*x*-*z* and *y*-*z* planes) at the center or about the center frequencies (2.45 GHz and 6.1 GHz) of the low and high bands are plotted. Since the $TM_{1/2,1/2}$ mode with two orthogonal quarter-wavelength resonances is excited in the low band, the $E_\theta$ and $E_\varphi$ components are seen to be comparable at 2.45 GHz. Symmetric patterns in the *x*-*z* and *y*-*z* planes are also seen.

On the other hand, the $TM_{1/2,1/2}$-like mode is excited in the high band, which is modified by the coupling feed also contributing to the antenna radiation as discussed in Section II.

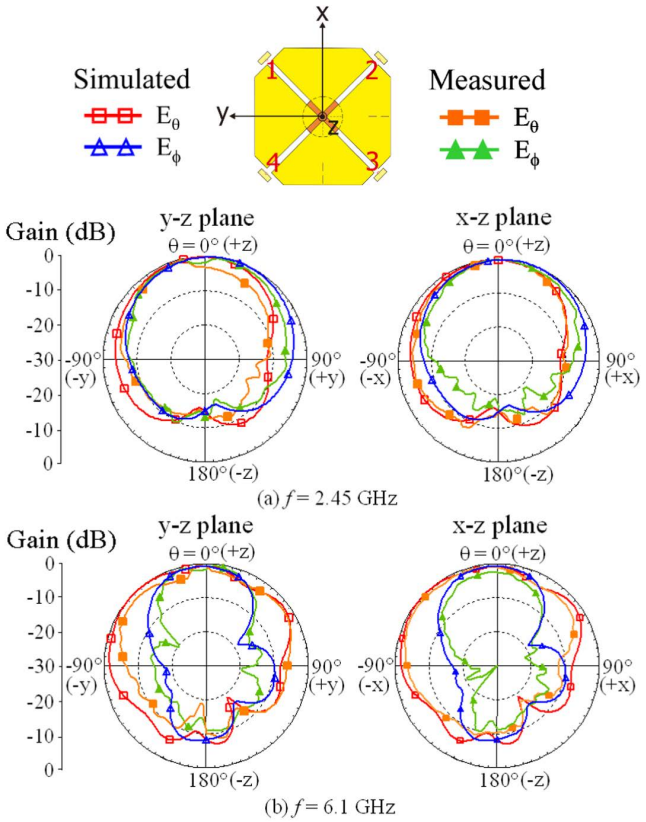


**FIGURE 21.** Measured and simulated normalized radiation patterns of Port 1. (a) 2.45 GHz. (b) 6.1 GHz.

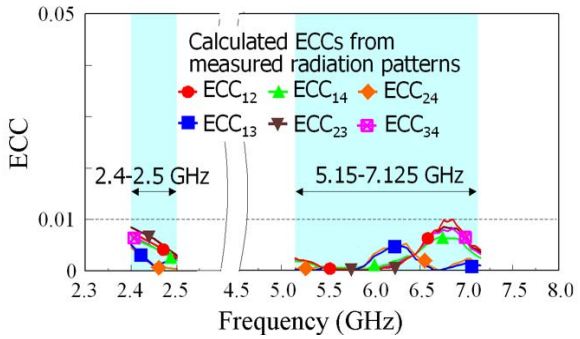


**FIGURE 22.** Calculated ECC based on measured three-dimensional radiation patterns.

This makes the $E_\theta$ component relatively much stronger than the $E_\phi$ component as seen in the radiation patterns at 6.1 GHz. Both the measured and simulated results also agree well.

Fig. 22 shows the calculated ECC by applying the measured amplitudes and phases of the electric fields in the three-dimensional radiation patterns [31], [33]. The corresponding radiation-based equation given in [33] is applied. The obtained ECCs between the radiation patterns of Ports 1, 2 ($ECC_{12}$), Ports 1, 3 ($ECC_{13}$), Ports 1, 4 ($ECC_{14}$), Ports 2, 3 ($ECC_{23}$), Ports 2, 4 ($ECC_{24}$), and Ports 3, 4 ($ECC_{34}$) are less than 0.01 in both the low and high bands. Note that the corresponding simulated results obtained using the simulated (ANSYS HFSS [29]) electric fields in the radiation patterns are lower than 0.001. The simulated ECCs are not shown

in the figure for comparison. Even with the ECCs results shown in Fig. 22 less than 0.01, the four radiated waves of the four ports in the proposed antenna can be considered to be uncorrelated.

## VI. CONCLUSION

A four-port square patch MIMO antenna having attractive features of all-metal structure, small patch size ($0.41\lambda \times 0.41\lambda$ at 2.45 GHz), high port isolation ($> 20$ dB), low radiation correlation (ECC $< 0.01$), and high antenna efficiency ($> 86\%$) in the 2.4 GHz and 5/6 GHz WiFi-6E bands has been proposed. The decoupling techniques of the hybrid metal walls and half-wavelength diagonal open-slots applied in the proposed antenna have been demonstrated to achieve enhanced port isolation of the four ports to generate four uncorrelated waves. The operating principle and design considerations of the proposed antenna have been addressed. A parametric study for fine adjustment of the antenna's design dimensions has been presented. The experimental results of the fabricated prototype have also been shown to verify the simulation results. With the obtained antenna performance, the proposed four-port square patch antenna will be promising for WiFi-6E $4 \times 4$ MIMO access-point application to cover the 2.4 GHz and 5/6 GHz bands.

## REFERENCES

[1] D. Manteuffel and R. Martens, "Compact multimode multielement antenna for indoor UWB massive MIMO," *IEEE Trans. Antennas Propag.*, vol. 64, no. 7, pp. 2689–2697, Jul. 2016.

[2] W. Su, Q. Zhang, S. Alkaraki, Y. Zhang, X.-Y. Zhang, and Y. Gao, "Radiation energy and mutual coupling evaluation for multimode MIMO antenna based on the theory of characteristic mode," *IEEE Trans. Antennas Propag.*, vol. 67, no. 1, pp. 74–84, Jan. 2019.

[3] K.-L. Wong, J.-Z. Chen, and W.-Y. Li, "Four-port wideband annular-ring patch antenna generating four decoupled waves for 5G multi-input–multi-output access points," *IEEE Trans. Antennas Propag.*, vol. 69, no. 5, pp. 2946–2951, May 2021.

[4] K.-L. Wong, X.-Q. Ye, and W.-Y. Li, "Wideband four-port single-patch antenna based on the quasi-TM1/2,1/2 mode for 5G MIMO access-point application," *IEEE Access*, vol. 10, pp. 9232–9240, 2022.

[5] E. Antonino-Daviu, M. Cabedo-Fabres, M. Gallo, M. Ferrando-Bataller, and M. Bozzetti, "Design of a multimode MIMO antenna using characteristic modes," in *Proc. 3rd Eur. Conf. Antennas Propag.*, Berlin, Germany, Mar. 2009, pp. 1840–1844.

[6] J.-S. Row, S.-H. Yeh, and K.-L. Wong, "A wide-band monopolar plate-patch antenna," *IEEE Trans. Antennas Propag.*, vol. 50, no. 9, pp. 1328–1330, Sep. 2002.

[7] M. Ikram, M. S. Sharawi, and A. Shamim, "Compact circular connected monopole antenna arrays for wideband MIMO applications," *IET Microw., Antennas Propag.*, vol. 12, no. 13, pp. 2122–2127, Oct. 2018.

[8] A. A. R. Saad and H. A. Mohamed, "Conceptual design of a compact four-element UWB MIMO slot antenna array," *IET Microw., Antennas Propag.*, vol. 13, no. 2, pp. 208–215, 2019.

[9] D. Sipal, M. P. Abegaonkar, and S. K. Koul, "Easily extendable compact planar UWB MIMO antenna array," *IEEE Antennas Wireless Propag. Lett.*, vol. 16, pp. 2328–2331, 2017.

[10] G. Srivastava and A. Mohan, "Compact MIMO slot antenna for UWB applications," *IEEE Antennas Wireless Propag. Lett.*, vol. 15, pp. 1057–1060, 2016.

[11] R. Anitha, P. V. Vinesh, K. C. Prakash, P. Mohanan, and K. Vasudevan, "A compact quad element slotted ground wideband antenna for MIMO applications," *IEEE Trans. Antennas Propag.*, vol. 64, no. 10, pp. 4550–4553, Oct. 2016.

[12] E. Fritz-Andrade, A. Perez-Miguel, R. Gomez-Villanueva, and H. Jardon-Aguilar, "Characteristic mode analysis applied to reduce the mutual coupling of a four-element patch MIMO antenna using a defected ground structure," *IET Microw., Antennas Propag.*, vol. 14, no. 2, pp. 215–226, Feb. 2020.

[13] A. Ramachandran, S. V. Pushpakaran, M. Pezholil, and V. Kesavath, "A four-port MIMO antenna using concentric square-ring patches loaded with CSRR for high isolation," *IEEE Antennas Wireless Propag. Lett.*, vol. 15, pp. 1196–1199, 2016.

[14] H. Li, J. Xiong, and S. He, "A compact planar MIMO antenna system of four elements with similar radiation characteristics and isolation structure," *IEEE Antennas Wireless Propag. Lett.*, vol. 8, pp. 1107–1110, 2009.

[15] I. R. R. Barani, K.-L. Wong, Y.-X. Zhang, and W.-Y. Li, "Low-profile wideband conjoined open-slot antennas fed by grounded coplanar waveguides for $4 \times 4$ 5G MIMO operation," *IEEE Trans. Antennas Propag.*, vol. 68, no. 4, pp. 2646–2657, Apr. 2020.

[16] D. Q. Liu, H. J. Luo, M. Zhang, H. L. Wen, B. Wang, and J. Wang, "An extremely low-profile wideband MIMO antenna for 5G smartphones," *IEEE Trans. Antennas Propag.*, vol. 67, no. 9, pp. 5772–5780, Sep. 2019.

[17] K.-L. Wong, C.-J. Chen, and W.-Y. Li, "Integrated four low-profile shorted patch dual-band WLAN MIMO antennas for mobile device applications," *IEEE Trans. Antennas Propag.*, vol. 69, no. 6, pp. 3566–3571, Jun. 2021.

[18] L. Chang and H. Wang, "Miniaturized wideband four-antenna module based on dual-mode PIFA for 5G $4\times4$ MIMO applications," *IEEE Trans. Antennas Propag.*, vol. 69, no. 9, pp. 5297–5304, Sep. 2021.

[19] K. L. Wong, M. F. Jian, and W. Y. Li, "Low-profile wideband four-corner-fed square patch antenna for 5G MIMO mobile antenna application," *IEEE Antennas Wireless Propag. Lett.*, vol. 20, no. 12, pp. 2054–2058, Dec. 2021.

[20] *Unlicensed Use of the 6 GHz Band*. Federal Communications Commission Fact Sheet. Accessed: Apr. 2, 2020. [Online]. Available: https://docs.fcc.gov/public/attachments/DOC-363490A1.pdf

[21] C.-A. Cai, K.-Y. Kai, and W.-J. Liao, "A WLAN/WiFi-6E MIMO antenna design for handset devices," in *Proc. Int. Symp. Antennas Propag. (ISAP)*, Taiwan, Oct. 2021, pp. 1–2.

[22] P. Mathur, R. Augustine, M. Gopikrishna, and S. Raman, "Dual MIMO antenna system for 5G mobile phones, 5.2 GHz WLAN, 5.5 GHz WiMAX and 5.8/6 GHz WiFi applications," *IEEE Access*, vol. 9, pp. 106734–106742, 2021.

[23] W.-C. Jhang and J.-S. Sun, "Small antenna design of triple band for WiFi 6E and WLAN applications in the narrow border laptop computer," *Int. J. Antennas Propag.*, vol. 2021, pp. 1–8, Jul. 2021.

[24] K. L. Wong, G. L. Yan, and W. Y. Li, "Conjoined yet decoupled wideband multiantenna MIMO linear patch array," *IEEE Access*, vol. 10, pp. 46302–46311, 2022.

[25] S. W. Su, K. L. Wong, and C. L. Tang, "Band-notched ultra-wideband planar monopole antenna," *Microw. Opt. Technol. Lett.*, vol. 44, pp. 217–219, Feb. 2005.

[26] K.-L. Wong, B.-W. Lin, and S.-E. Lin, "High-isolation conjoined loop multi-input multi-output antennas for the fifth-generation tablet device," *Microw. Opt. Technol. Lett.*, vol. 61, no. 1, pp. 111–119, Jan. 2019.

[27] K.-L. Wong, Y.-H. Chen, and W.-Y. Li, "Conjoined ultra-wideband (2,300–6,000 MHz) dual antennas for LTE HB/WiFi/5G multi-input multi-output operation in the fifth-generation tablet device," *Microw. Opt. Technol. Lett.*, vol. 61, no. 8, pp. 1958–1963, Aug. 2019.

[28] *Flat Wire Inductor Calculator, Chemandy Electronics*. Accessed: Mar. 1, 2022. [Online]. Available: https://chemandy.com/calculators/flat-wire-inductor-calculator.htm

[29] *3D High Frequency Electromagnetic Simulation Software, ANSYS HFSS*. Accessed: Mar. 1, 2022. [Online]. Available: https://www.ansys.com/products/electronics/ansys-hfss

[30] M. Manteghi and Y. Rahmat-Samii, "Multiport characteristics of a wideband cavity backed annular patch antenna for multipolarization operations," *IEEE Trans. Antennas Propag.*, vol. 53, no. 1, pp. 466–474, Jan. 2005.

[31] K. L. Wong and G. L. Yan, "Wideband three-port equilateral triangular patch antenna generating three uncorrelated waves for 5G MIMO access points," *IEEE Access*, vol. 10, pp. 893–899, 2022.

[32] Y. Okano and K. Cho, "Antenna measurement system for mobile terminals," *NTT DoCoMo Tech. J.*, vol. 9, no. 2, pp. 43–50, 2007.

[33] M. S. Sharawi, "Printed multi-band MIMO antenna systems and their performance metrics," *IEEE Antennas Propag. Mag.*, vol. 55, no. 5, pp. 218–232, Oct. 2013.

**KIN-LU WONG** (Fellow, IEEE) received the B.S. degree in electrical engineering from the National Taiwan University, Taipei, Taiwan, in 1981, and the M.S. and Ph.D. degrees in electrical engineering from Texas Tech University, Lubbock, TX, USA, in 1984 and 1986, respectively.

From 1986 to 1987, he was a Visiting Scientist with the Max-Planck-Institute for Plasma Physics, Munich, Germany. Since 1987, he has been with the Department of Electrical Engineering, National Sun Yat-sen University (NSYSU), Kaohsiung, Taiwan, where he became a Professor, in 1991. From 1998 to 1999, he was a Visiting Scholar with the ElectroScience Laboratory, The Ohio State University, Columbus, OH, USA. He was elected to be a Sun Yat-sen Chair Professor at NSYSU, in 2005, a Distinguished Chair Professor at NSYSU, in 2017, and the National Chair Professor of Ministry of Education of Taiwan, in 2016. He also served as the Chairperson for the Department of Electrical Engineering, from 1994 to 1997, the Vice President for research affairs, from 2005 to 2007, and the Senior Vice President at NSYSU, from 2007 to 2012. He is currently the National Chair Professor of the Ministry of Education, a Distinguished Researcher of Ministry of Science and Technology, and a Distinguished Chair Professor with NSYSU. He has authored more than 580 refereed journal articles and 300 conference papers and has personally supervised 57 graduated Ph.D. He holds over 300 patents, including 103 U.S. patents. He is the author of *Design of Nonplanar Microstrip Antennas and Transmission Lines* (Wiley, 1999), *Compact and Broadband Microstrip Antennas* (Wiley, 2002), and *Planar Antennas for Wireless Communications* (Wiley, 2003). His published articles have been cited over 33,700 times with an H-index of 87 in Google Scholar.

Dr. Wong served or currently serves as an IEEE AP-S AdCom Member, an IEEE TRANSACTIONS ON ANTENNAS AND PROPAGATION Track Editor/Associate Editor, an IEEE TRANSACTIONS ON ANTENNAS AND PROPAGATION Paper Awards Committee Member, and an AP-S Field Awards Committee Member. He received the Outstanding Research Award three times (1995, 2000, and 2002) from the Taiwan National Science Council. He also received the Outstanding Electrical Engineering Professor Award (2003) from the Institute of Electrical Engineers of Taiwan and the Outstanding Engineering Professor Award (2004) from the Institute of Engineers of Taiwan. In 2008, the research achievements on handheld device antennas of NSYSU Antenna Laboratory led by him was selected to be top 50 scientific achievements of Taiwan Ministry of Science and Technology in past 50 years (1959–2009). He was a recipient of the 2010 Outstanding Research Award of Pan Wen Yuan Foundation and selected as top 100 Honor of Taiwan by Global Views Monthly, in August 2010, for his contribution in mobile antenna researches. He was also a recipient of the Academic Award (2012) from the Taiwan Ministry of Education and the Outstanding Distinguished Researcher Award (2013) from the Taiwan Ministry of Science and Technology. He and his graduate students have been awarded the Best Paper Award (APMC Prize) from 2008 APMC and the Best Student Paper Award/Young Scientist Award from 2007 ISAP, 2008 APMC, 2009 ISAP, 2010 ISAP, 2012 ISAP, and 2016 ISAP. His graduate students also won the First Prize of 2007 and 2009 Taiwan National Mobile Handset Antenna Design Competition. He was awarded the Best Associate Editor two times (2015 and 2016) for the IEEE TRANSACTIONS ON ANTENNAS AND PROPAGATION. He was also a PE7 Panel Member of 2015, 2017, and 2019 European Research Council Advanced Grant Panel and a Chief Consultant of the Institute of Antenna Engineers of Taiwan. He also served as the Chair of the Judge Panel (2014–2021) of the National Communication Antenna Design Competition organized by the Taiwan Ministry of Economics. He served as the General Chair for 2012 APMC, 2014 ISAP, and 2016 APCAP, Kaohsiung. He was elected as a Thomson Reuters Highly Cited Researcher, in both 2014 and 2015, and also elected as an Elsevier Most Cited Researcher, in 2015. In 2022, he was selected by Research.com to be ranked #99 in Full World Ranking and #1 in Full Taiwan Ranking in the 2022 Edition of Ranking of Top 1000 Scientists in the field of Electronics and Electrical Engineering. He is a Thomson Reuters Highly Cited Researcher and an Elsevier Most Cited Researcher.

**HONG-YU JIANG** (Student Member, IEEE) received the B.S. degree in electrical engineering from the National Taiwan Ocean University, Keelung, Taiwan, and the M.S. degree in electrical engineering from the National Sun Yat-sen University, Kaohsiung, Taiwan. His main research interests include wideband MIMO multiport patch antennas and MIMO capacity/throughput testing techniques for 5G/B5G access-point and mobile-device applications.

**WEI-YU LI** (Member, IEEE) was born in Taipei, Taiwan, in 1981. He received the B.S. degree in electrical engineering from Feng Chia University, Taichung, Taiwan, in 2004, and the M.S. and Ph.D. degrees in electrical engineering from the National Sun Yat-sen University (NSYSU), Kaohsiung, Taiwan, in 2006 and 2009, respectively.

After graduated from NSYSU, in 2009, he has been with the Information and Communication Research Laboratories (ICL), Industrial Technology Research Institute (ITRI), Hsinchu, Taiwan, participating and leading advanced research for development of emerging wireless antenna technologies. From April 2012 to October 2012, he was as an Exchange Guest Researcher with the National Institute of Information and Communications Technology (NICT), Tokyo, Japan. He is currently a Deputy Technology Manager at ITRI. He has authored or coauthored 30 refereed journal articles and 40 conference papers. He holds over 70 patents, including U.S., Taiwan, and EU patents. His published articles have been cited over 1,380 times with an H-index of 22 in Google Scholar.

Dr. Li has been selected as an International Steering Committee Member of 2019–2021 ISAP. He also served as an AdCom Member for the Institute of Antenna Engineers of Taiwan (2014, 2015, and 2018–2022). He also served as one member of the Judge Panel (2014 to 2022) for the National Terminal Antenna Design Competition organized by the Taiwan Ministry of Economics. He received the Young Scientist Award from 2007 ISAP and the Best Paper Award (APMC Prize) from 2008 APMC. He has been a principal investigator or co-principal investigator of many research projects in ITRI and has received numerous recognitions, including the First Prize of the Outstanding Research Award of ITRI, in 2010; the Solar Industrial Award (SIA) of Europe, in 2011; the Outstanding Innovation Award of ITRI, in 2013; the Second Prize of the Outstanding Research Award of ITRI, in 2014; the 2015 Research and Development 100 Award Finalist of the USA; the Outstanding Innovation Award of ITRI, in 2017; the First Prize of the Outstanding Industrialization Award of ITRI, in 2017; the Second Prize of the Outstanding Industrialization Award of ITRI, in 2020; and the Third Prize of the Outstanding Industrialization Award of ITRI, in 2021. He also received the Outstanding Lecturer Award of ITRI, in 2013; and the International Paper Award of ICL of ITRI, in 2020. He was the Chair of IEEE AP-S Tainan Chapter (2021–2022).